

Microlensing of collimated Gamma-Ray Burst afterglows

Kunihito Ioka¹ and Takashi Nakamura²

¹ Department of Physics, Kyoto University, Kyoto 606-8502, Japan

³Yukawa Institute for Theoretical Physics, Kyoto University, Kyoto 606-8502, Japan

Dec 2 2000

ABSTRACT

We investigate stellar microlensing of the collimated gamma-ray burst afterglows. A spherical afterglow appears on the sky as a superluminally expanding thin ring (“ring-like” image), which is maximally amplified as it crosses the lens. We find that the image of the collimated afterglow becomes quite uniform (“disk-like” image) after the jet break time (after the Lorentz factor of the jet drops below the inverse of the jet opening angle). Consequently, the amplification peak in the light curve after the break time is lower and broader, and even disappears at frequencies above the typical synchrotron frequency (optical and X-ray) but remains at low frequencies (radio). Therefore multi-band observations are important to constrain the cosmological density of the stellar mass objects. We also show that some proper motion and polarization is expected, peaking around the maximum amplification. A low peak in the optical light curve with the detection of the peak in the radio light curve, proper motion or polarization can test whether the afterglows are jets or not.

Subject headings:

1. INTRODUCTION

Whether the gamma-ray bursts (GRBs) are collimated or not is one of the most important questions in GRBs, since the jet configuration is crucial for almost all aspects of GRBs, such as the energetics, statistics, and central engine models of GRBs. There are several suggestions for the collimation of GRBs. When the Lorentz factor of the ejecta drops below the inverse of the opening angle, the ejecta begins to spread sideways, and we expect a break in the light curve of the afterglow (Rhoads 1999). Such breaks have been observed in several GRBs, such as GRB 990510 (Stanek et al. 1999, Harrison et al. 1999) and GRB 991216 (Halpern et al. 2000). The rapid decline rate (e.g., GRB 980519) or the

unusually slow decline rate of GRB 980425 also suggests the collimation of GRBs (Halpern et al. 1999, Sari, Piran & Halpern 1999, Nakamura 1999). However, in order to establish that the afterglows are jets, other observations are indispensable, such as early afterglow observations at radio frequencies (Frail et al. 2000). Microlensing of the afterglows has a potential to be one of such observations. The emission region of the afterglow seen by an external observer occupies a size of $\sim 10^{17}$ cm on the sky which is comparable to the lensing zone of a solar mass lens located at the cosmological distance (Loeb & Perna 1998). Therefore microlensing can resolve the afterglow, and hence we can expect that some features of jets can be obtained by the observations of the microlensed afterglows.

On the other hands, afterglows will be useful to constrain the cosmological density parameter of stellar mass objects Ω_* through microlensing. As a result of the relativistic motion, the emission region appears to expand superluminally, so that the microlensing time is only ~ 1 day (Loeb & Perna 1998). This is much shorter than that of common sources, $\gtrsim 10$ years (Gould 1995). The microlensing probability of a source at a redshift $z_s \sim 3$ is $\sim 0.3\Omega_*$ (Press & Gunn 1973, Gould 1995, Koopmans & Wambsganss 2000). Since the known luminous stars amount to $\Omega_* \gtrsim 4 \times 10^{-3}$ (Fukugita, Hogan & Peebles 1998), roughly 1 in $\sim 10^3$ GRBs would be within the lensing zone. If some fraction of the dark matter is made of massive compact halo objects (MACHOs), as Galactic microlensing searches suggest (Alcock et al. 2000), we can expect higher probability. Remarkably, the microlensed afterglow may have been already observed in the light curve of GRB 000301C as the achromatic bump (Garnavich, Loeb & Stanek 2000). Since new GRB satellites such as *HETE-2* and *SWIFT* will provide many opportunities to monitor afterglows frequently, it is important to study the jet effects on the microlensing of the GRB afterglows.¹

In §2 and 3, we will calculate the equal arrival time surfaces, and the surface brightness distribution of the afterglow image, respectively, taking into account of the jet effects. In §4, we will calculate the microlensed light curve. In §5, we will investigate the proper motion and the polarization induced by microlensing. §6 is devoted to summary and discussions.

2. EQUAL ARRIVAL TIME SURFACE

Let E , ρ , θ_i and c_s be the burst energy, the density of the ambient gas, the initial opening angle, and the sound speed of the jet, respectively. The Lorentz factor of the shock

¹ When we have almost completed this work, Mao & Loeb (2000) informed us that Granot & Loeb (2000) are performing a similar (but perhaps more detail) calculation.

front approximately evolves as

$$\Gamma = \begin{cases} \Gamma_b (r/r_b)^{-3/2}, & r < r_b, \\ \Gamma_b \exp \{-(r - r_b)/r_\Gamma\}, & r > r_b, \end{cases} \quad (1)$$

where $r_b = (75E/8\pi\rho c_s^2)^{1/3} = 3.9 \times 10^{18} E_{52}^{1/3} n_1^{-1/3} (\sqrt{3}c_s/c)^{-2/3} \text{cm}$, $r_\Gamma = (8/75)^{1/3} r_b$ and $\Gamma_b = 2c_s/5c\theta_i$ (Rhoads 1999). Here E_{52} is the burst energy in units of 10^{52} ergs, and n_1 is the ambient gas density in cm^{-3} . We assume that the material is uniformly distributed across the jet at any r , the emission comes just behind the shock front, and $\Gamma \gg 1$. Such approximations are sufficient and convenient to understand the key features before performing more detail calculations (Rhoads 1999, Panaiteescu & Mészáros 1999, Moderski, Sikora & Bulik 2000, Huang, Dai & Lu 2000, Granot, Piran & Sari 1999).

The arrival time T of a photon emitted at an angle θ from the line of sight is given by $T = t - r\mu/c$ where $t = \int dr/c\sqrt{1-\Gamma^{-2}}$ and $\mu = \cos\theta$. This relation with equation (1) can be written as

$$1 - \mu = \begin{cases} \frac{1}{8\Gamma_b^2} \left(\frac{r}{r_b}\right)^{-1} \left[\frac{T}{T_b} - \left(\frac{r}{r_b}\right)^4 \right], & r < r_b, \\ \frac{1}{8\Gamma_b^2} \left(\frac{r}{r_b}\right)^{-1} \left[\frac{T}{T_b} - 1 - \frac{2r_\Gamma}{r_b} \left[\exp \left\{ \frac{2(r-r_b)}{r_\Gamma} \right\} - 1 \right] \right], & r > r_b, \end{cases} \quad (2)$$

where $T_b = r_b/8c\Gamma_b^2 = 0.35E_{52}^{1/3} n_1^{-1/3} (\sqrt{3}c_s/c)^{-8/3} (\theta_i/0.01)^2 \text{days}$. Equation (2) gives the equal arrival time surface at T , and some examples are shown in Figure 1. In the power law regime, $T \lesssim T_b$, the apparent size $r_{\perp,max}$ of the jet is determined by the equal arrival time surface (Sari 1998, Panaiteescu & Mészáros 1998). The distance of the equal arrival time surface from the line of sight is given by $r_\perp = r\sqrt{1-\mu^2} \simeq r\sqrt{2(1-\mu)}$ with equation (2), which takes the maximum value of $r_{\perp,max} = (T/5T_b)^{5/8} r_b/\Gamma_b = 1.2 \times 10^{17} E_{52}^{1/8} n_1^{-1/8} (\theta_i/0.01)^{-1/4} (T/1\text{day})^{5/8} \text{cm}$ at $r/r_b = (T/5T_b)^{1/4}$. On the other hand, in the exponential regime, $T \gtrsim T_b$, the apparent size of the jet is determined by the opening angle of the jet, $\theta_b = \theta_i + c_s t_{co}/r$, where $t_{co} = \int dr/c\Gamma$ is the comoving time in the jet frame. With equation (1), we find

$$\frac{\theta_b}{1/\Gamma_b} = \begin{cases} \frac{2}{5} \frac{c_s}{c} \left[1 + \left(\frac{r}{r_b}\right)^{3/2} \right], & r < r_b, \\ \frac{2}{5} \frac{c_s}{c} \left[1 + \left(\frac{r}{r_b}\right)^{-1} \left\{ 1 + \frac{5r_\Gamma}{2r_b} \left[\exp \left\{ \frac{(r-r_b)}{r_\Gamma} \right\} - 1 \right] \right\} \right], & r > r_b. \end{cases} \quad (3)$$

If the direction of the jet axis is $(\theta, \phi) = (\theta_0, 0)$ with $\theta = 0$ being the line of sight, the edge of the jet is given by $\theta^2 + \theta_0^2 - 2\theta\theta_0 \cos\phi = \theta_b^2$. In Figure 1, the trajectories of jet edges for $\theta_0 = 0$ and $\theta_0 = \theta_i$ on the $\phi = 0$ plane are plotted. We can see that there is an intermediate regime where the evolution of the Lorentz factor is power law while the edge of the jet determines the apparent size (Rhoads 1999, Panaiteescu & Mészáros 1999).

3. SURFACE BRIGHTNESS DISTRIBUTION

Let us consider a system that have an isotropic luminosity dL_ν in its rest frame and is moving with Lorentz factor γ in a direction (θ, ϕ) with a solid angle $d\Omega = d\mu d\phi$. Emitted photon with frequency ν is blueshifted to frequency $\nu/\gamma(1 - \beta\mu)$, where $\beta = \sqrt{1 - \gamma^{-2}}$. Using the Lorentz transformation, the observed flux at distance D and frequency ν is given by $dF_\nu = dL_{\nu\gamma(1-\beta\mu)}/4\pi D^2\gamma^3(1 - \beta\mu)^3$. A jet, with a luminosity L_ν in its local frame, is a collection of such systems, so that we have $dL_\nu = L_\nu d\Omega/\pi\theta_b^2$ with equation (3). Now we assume that the luminosity in the local frame is $L_\nu \propto \Gamma^a\nu^b$. Then, the flux per unit area, i.e., the surface brightness $S(r_\perp, \phi; T) := d^2F_\nu/r_\perp dr_\perp d\phi$ can be obtained by

$$S(r_\perp, \phi; T) \propto \Gamma^{a+b-3}(1 - \beta\mu)^{b-3}\theta_b^{-2}\frac{d\mu}{dr} \left/ \left| \frac{dr_\perp^2}{dr} \right| \right., \quad (4)$$

where we use $d\Omega/r_\perp dr_\perp d\phi = 2d\mu/dr_\perp^2$ and the fact that the Lorentz factor of the shock front Γ is higher than that of the material behind it γ by a factor of $\sqrt{2}$ (Blandford & McKee 1976). With equations (1), (2) and (3), we can find that equation (4) is a function of r , noting $r_\perp \simeq r\sqrt{2(1 - \mu)}$ and $1 - \beta\mu \simeq 1 - \beta + 1 - \mu \simeq 1/\Gamma^2 + 1 - \mu$. Since we can obtain r for given r_\perp by $r_\perp \simeq r\sqrt{2(1 - \mu)}$ with equation (2), the surface brightness can be calculated as a function of r_\perp . Note that there are two solutions of r for each r_\perp , one from the front of the equal arrival time surface and the other from its back. As time goes, the emission from the back does not contribute due to the jet geometry, as we can see from Figure 1.

The assumption $L_\nu \propto \Gamma^a\nu^b$ is valid for frequencies far from the typical synchrotron frequency ν_m (Sari, Piran & Narayan 1998, Sari, Piran & Halpern 1999). For simplicity, we neglect scattering, self-absorption, and electron cooling. Then, the luminosity is proportional to the total number of swept-up electrons $N_e \propto \Gamma^{-2}$ (Rhoads 1999) times the radiation power from each electron $P \propto \gamma^2 B^2 \propto \Gamma^4$. Since the typical frequency is $\nu_m \propto B\gamma^2 \propto \Gamma^3$, the luminosity at the typical frequency is $L_{\nu_m} \propto \Gamma^{-1}$. At $\nu \ll \nu_m$, we have $L_\nu = L_{\nu_m}(\nu/\nu_m)^{1/3} \propto \Gamma^{-2}\nu^{1/3}$. At $\nu \gg \nu_m$, if electrons are accelerated to a power law distribution with index p , we have $L_\nu = L_{\nu_m}(\nu/\nu_m)^{-(p-1)/2} \propto \Gamma^{(3p-5)/2}\nu^{-(p-1)/2}$. Therefore, we find $a = -2$, $b = 1/3$ at $\nu \ll \nu_m$, and $a = (3p-5)/2$, $b = -(p-1)/2$ at $\nu \gg \nu_m$. We shall adopt $p = 2.5$.

In Figure 2, we show the surface brightness distribution as a function of the distance from the center for $\theta_0 = 0$ (the jet axis coincides with the line of sight). In the power law regime $T/T_b \lesssim 1$, the surface brightness is brighter near the edge and dimmer at the center, i.e., “ring-like” (Waxman 1997, Sari 1998, Panaitescu & Mészáros 1998). However, in the exponential regime $T/T_b \gtrsim 1$, the surface brightness becomes nearly constant, i.e., “disk-like”. The qualitative feature does not depend on θ_0 . In the intermediate regime, a

part of the ring will be missing due to the jet edge when $\theta_0 \neq 0$.

4. MICROLENSED LIGHT CURVE

We now consider a point mass lens of mass M that is located at L from the source center on the sky. The Einstein radius on the source plane is given by $R_E = [(4GM/c^2)(D_s D_{ls}/D_l)]^{1/2}$, with D_l , D_s and D_{ls} being the angular diameter distance to the lens, to the source, and from the lens to the source, respectively. A point lens is described by three parameters, the Einstein radius, $r_E := R_E/(r_b/\Gamma_b) = 0.45 (M/M_\odot)^{1/2} [(D_s D_{ls}/D_l)/10^{28}\text{cm}]^{1/2} E_{52}^{-1/3} n_1^{1/3} (\sqrt{3}c_s/c)^{5/3} (\theta_i/0.01)^{-1}$, the impact parameter, $l := L/(r_b/\Gamma_b)$, and the azimuthal angle of the lens position, ϕ_l , with respect to the source center on the sky. Here we measure the distance from the line of sight in units of r_b/Γ_b .

The observed flux can be calculated numerically by $F_\nu = \int A(r_\perp, \phi) S(r_\perp, \phi; T) r_\perp dr_\perp d\phi$, where $A(r_\perp, \phi) = (u_l^2 + 2)/u_l \sqrt{u_l^2 + 4}$ and $u_l = [L^2 + r_\perp^2 - 2Lr_\perp \cos(\phi - \phi_l)]^{1/2}/R_E$. The unlensed flux can be obtained by putting $A = 1$. In Figure 3, the lensed flux of an afterglow, the unlensed flux, and the lensed flux with keeping the initial surface brightness (i.e., keeping the “ring-like” image) are plotted by solid, dashed, and dotted lines, respectively. Only the exponential regime $T \gtrsim T_b$ is depicted, where the slope of the unlensed light curve is $-p = -2.5$ at $\nu \gg \nu_m$, and $-1/3$ at $\nu \ll \nu_m$ (Sari, Piran & Halpern 1999). At early times, the temporal profiles of the lensed and unlensed flux have the same shape but different amplitudes, since the source can be regarded as pointlike. The offset between the lensed and unlensed flux is a function of l/r_E . The maximum amplification occurs around when the edge of the image crosses the lens, $r_{\perp, \text{max}} \sim L = lr_b/\Gamma_b$. Here we set $l = 1$ so that the maximum amplification occurs at $T \sim 10T_b$, with the image being “disk-like”. In the upper panel of Figure 3, we consider the case $\nu \gg \nu_m$. At the maximum amplification, an amplification peak would appear if the image were “ring-like”, as in the power law regime² (Loeb & Perna 1998). However, since the image is “disk-like”, the amplification peak becomes lower and broader, and consequently disappears at $\nu \gg \nu_m$. At $\nu \ll \nu_m$, as shown in the lower panel of Figure 3, the amplification peak becomes lower but remains in the light curve even if the image is “disk-like”. This is because the the decline rate of the unlensed flux at $\nu \gg \nu_m$ is too steep ($-p = -2.5$) for the time derivative of the flux to be positive, but the slope at $\nu \ll \nu_m$ is enough mild ($-1/3$). Note that the amplification factor is nearly the same in both cases. In the intermediate regime, where the evolution

² This statement may depend on the more detail profile of the ring (Granot et al. 1999).

of the Lorentz factor is power law but the edge of the jet determines the image size, the amplification depends on the lens position ϕ_l when $\theta_0 \neq 0$. If the lens is located on the side where the ring is cut off by the jet edge, the amplification peak is small, while, if the lens is on the other side, the peak is relatively large.

5. PROPER MOTION AND POLARIZATION

Even when the multiple images formed by microlensing can not be resolved, the centroid of the combined image is expected to move. The order of the maximum displacement is estimated by $R_E/D_s \sim 10^{-11}(M/M_\odot)^{1/2} \sim 2(M/M_\odot)^{1/2}\mu\text{as}$ with $R_E \sim 10^{17}(M/M_\odot)^{1/2}\text{cm}$ and $D_s \sim 10^{28}\text{cm}$. This proper motion might be measured by the upcoming missions, such as the Space Interferometry Mission (SIM; see <http://sim.jpl.nasa.gov>), with positional accuracy down to $\sim 1\mu\text{as}$ (Paczyński 1998). To neglect the proper motion due to the jet edge effect (Sari 1999), we set here $\theta_0 = 0$. We can calculate the light centroid numerically by weighting the image positions with brightness (Walker 1995, Mao & Witt 1998). The upper panel of Figure 4 shows the proper motion as a function of time at $\nu \gg \nu_m$. Initially, since the source is pointlike, the initial displacement is a function of l/r_E (see Figure 1 in Walker 1995). As the source expands, the centroid moves toward the lens due to the finite source effect (Mao & Witt 1998). The centroid goes through the origin in coincidence with the maximum amplification. It is important to note that the magnitude of the displacement does not depend on the surface brightness distribution of the image so much.

We also expect some polarization in the microlensed afterglows (Loeb & Perna 1998). Here, following Sari (1999), we shall consider the favorite conditions in which the polarization at each point in the image is $\Pi_0 = (p+1)/(p+7/3) \simeq 72\%$ toward the source center. To neglect the polarization due to the jet edge effect (Ghisellini & Lazzati 1999, Sari 1999), we set here $\theta_0 = 0$. The net polarization can be calculated by averaging $\Pi_0 \cos(2\phi)$ with $A(r_\perp, \phi)S(r_\perp, \phi; T)$. The lower panel of Figure 4 shows the net polarization as a function of time at $\nu \gg \nu_m$. The polarization has a maximum toward the lens in coincidence with the maximum amplification. Even in the exponential regime, the polarization due to microlensing is comparable to the polarization which is expected around the jet break time when $\theta_0 \neq 0$ (see Figure 4 in Sari 1999).

6. SUMMARY AND DISCUSSIONS

We have investigated stellar microlensing of collimated GRB afterglows taking into account of the jet effects. Using the analytical expressions for the evolution of the jet, we have first calculated the surface brightness distribution of the jet. We find that the image is “disk-like” after the jet break time, rather than “ring-like” before the break time. We have further analyzed the microlensing signal in the light curve of the afterglow observed at frequencies far below and far above the typical synchrotron frequency ν_m , where the radio is in the low frequency for about 1 month,³ and the optical is in the high frequency after about 1 day. If the edge of the image crosses the lens before the break time, the microlensing signal appears as an achromatic amplification peak in the light curve (Loeb & Perna 1998). We find that, after the break time, the amplification peak becomes lower and broader because of the “disk-like” image. Although the exact peak shape may be relevant to more detail calculations, the amplification peak disappears at frequencies $\nu \gg \nu_m$ but remains at $\nu \ll \nu_m$. This means that only optical observation is not sufficient for constraining Ω_* . At the break time, the peak amplitude depends on the lens position.

Microlensing also induces the proper motion and the polarization of the afterglow in coincidence with the maximum amplification. The magnitude of the proper motion does not depend on the image profile so much, which might be detected by upcoming missions, such as SIM, with positional accuracy down to $\sim 1\mu\text{as}$. From the proper motion we can estimate the apparent size of the afterglow explicitly. The maximum polarization due to microlensing is comparable to the polarization which is expected around the jet break time (Sari 1999), even if the image is “disk-like”.

A low amplification peak in the optical can be used to test whether the afterglows are jets or not, if we can confirm that the afterglow is microlensed by other observations, such as radio, proper motion and polarization observations, since a low peak in the optical means that the image is “disk-like”.

We would like to thank H. Sato, S. Kobayashi and T. Chiba for useful discussions. This work was supported in part by Grant-in-Aid for Scientific Research Fellowship of the Japanese Ministry of Education, Science, Sports and Culture, No.9627 (KI) and by Grant-in-Aid of Scientific Research of the Ministry of Education, Culture, and Sports, No.11640274 (TN) and 09NP0801 (TN).

³ The radio scintillation is suppressed at $\nu \gtrsim 10$ GHz (Goodman 1997).

REFERENCES

Alcock, C. et al. 2000 (astro-ph/0001272)

Blandford, R. D., & McKee, C. F. 1976, *Phys. Fluids*, 19, 1130

Frail, D. A., et al. 2000, *ApJ*, 534, 559

Fukugita, M., Hogan, C. J., & Peebles, P. J. E. 1998, *ApJ*, 503, 518

Garnavich, P. M., Loeb, A., & Stanek, K. Z. 2000, *ApJL*, in press (astro-ph/0008049)

Ghisellini, G., & Lazzati, D. 1999, *MNRAS*, 309, L7

Goodman, J. 1997, *New Astron.*, 2, 449

Gould, A. 1995, *ApJ*, 455, 37

Granot, J., & Loeb, A. 2000, in preparation

Granot, J., Piran, T., & Sari, R. 1999, *ApJ*, 513, 679

Halpern, J. P., Kemp, J., Piran, T., & Bershadsky, M. A. 1999, *ApJ*, 517, L105

Halpern, J. P., et al. 2000, *ApJ*, in press (astro-ph/0006206)

Harrison, F. A., et al. 1999, *ApJ*, 523, L121

Huang, Y. F., Dai, Z. G., & Lu, T. 2000, *A&A*, 355, L43

Koopmans, L. V. E., & Wambsganss, J. 2000, astro-ph/0011029

Loeb, A., & Perna, R. 1998, *ApJ*, 495, 597

Mao, S., & Loeb, A. 2000, *ApJL*, submitted (astro-ph/0010029)

Mao, S., & Witt, H. J. 1998, *MNRAS*, 300, 1041

Moderski, R., Sikora, M., & Bulik, T. 2000, *ApJ*, 529, 151

Nakamura, T. 1999, *ApJ*, 522, L101

Paczynski, B. 1998, *ApJ*, 494, L23

Panaitescu, A., & Mészáros, P. 1998, *ApJ*, 493, L31

Panaitescu, A., & Mészáros, P. 1999, *ApJ*, 526, 707

Press, W. H., & Gunn, J. E. 1973, *ApJ*, 185, 397

Rhoads, J. E. 1999, *ApJ*, 525, 737

Sari, R. 1998, *ApJ*, 494, L49

Sari, R. 1999, *ApJ*, 524, L43

Sari, R., Piran, T., & Halpern, J. P. 1999, *ApJ*, 519, L17

Sari, R., Piran, T., & Narayan, R. 1998, ApJ, 497, L17

Stanek, K. Z., et al. 1999, ApJ, 522, L39

Walker, M. A. 1995, ApJ, 453, 37

Waxman, E. 1997, ApJ, 491, L19

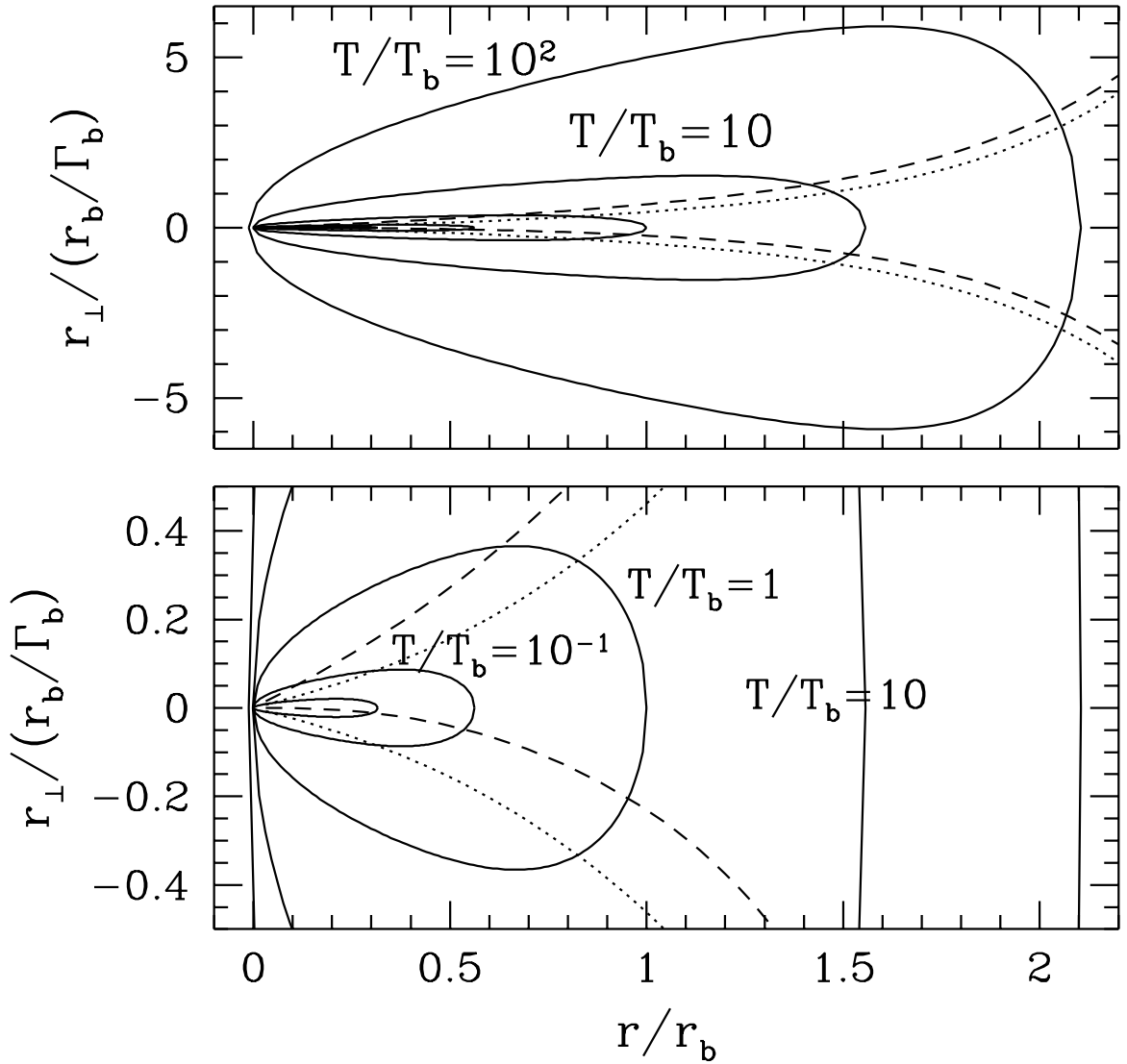


Fig. 1.— Equal arrival time surfaces, i.e., the surfaces from which photons from a thin shell arrives at the same time T to the observer far on the right side, are shown by solid lines. We adopt $\theta_i = 0.01$ and $c_s = c/\sqrt{3}$. The upper and lower panels are the same, but the scale of the vertical axis is different. The arrival times are $T/T_b = 10^{-2}, 10^{-1}, 1, 10, 10^2$ as the surface gets larger. The Lorentz factor of the emitting shell obeys equation (1), in which the shell decelerates exponentially at $r > r_b$. The trajectories of the jet edges for $\theta_0 = 0$ and $\theta_0 = \theta_i$ are also plotted with dotted and dashed lines, respectively, with $\theta_0 = 0$ being the line of sight. No photon comes from the outside of these trajectories.

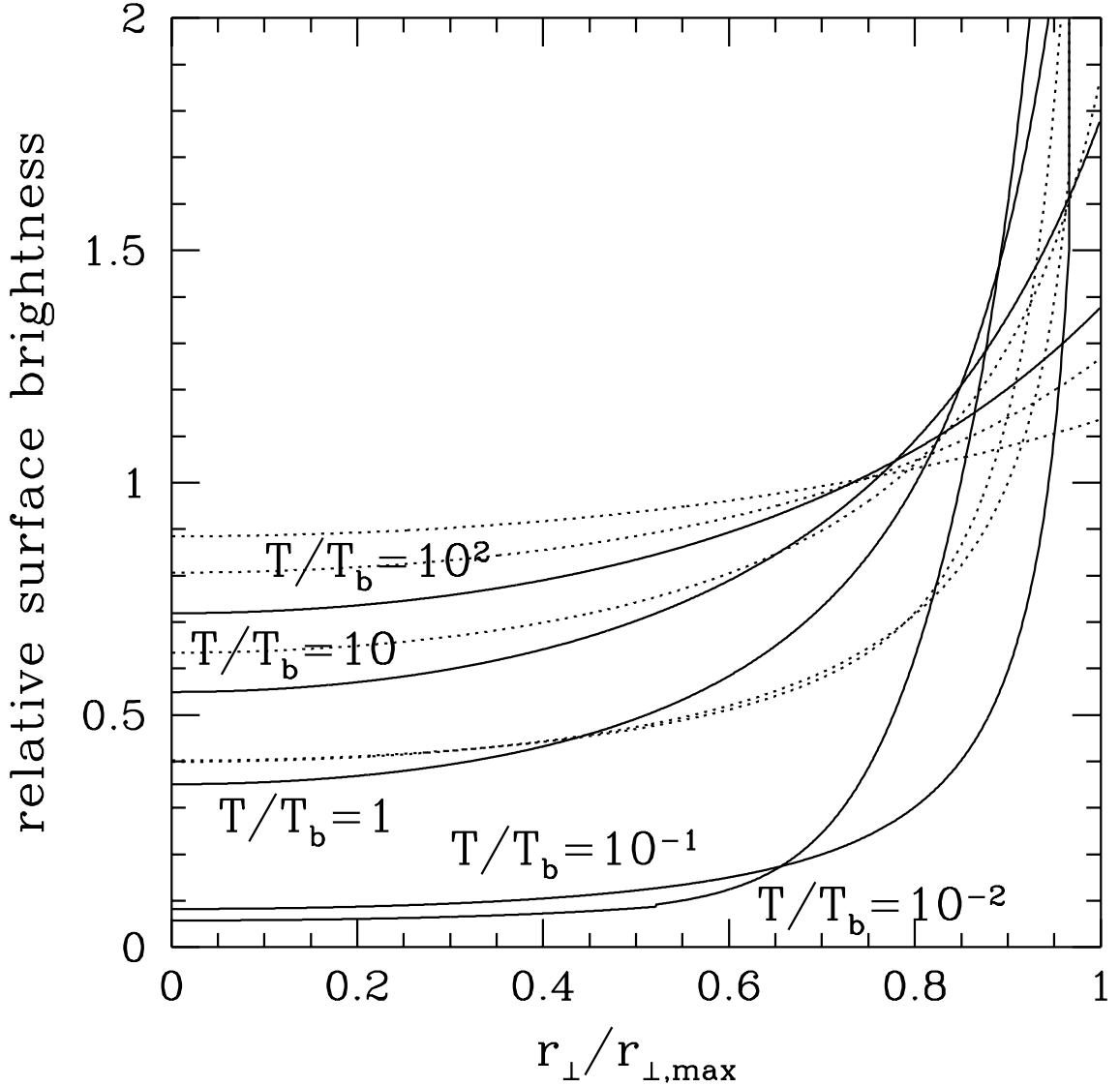


Fig. 2.— The surface brightness as a function of the distance from the center at the times $T/T_b = 10^{-2}, 10^{-1}, 1, 10, 10^2$ is shown for frequencies above and below the typical synchrotron frequency with solid and dotted lines, respectively. Each surface brightness is normalized by the average surface brightness. The relative brightness at the center increases with the time T . The image is “ring-like” at $T \lesssim T_b$ and “disk-like” at $T \gtrsim T_b$. The divergence of the brightness at $r_\perp = r_{\perp,\max}$ is an artifact of the assumption that the radiation comes from a two-dimensional shell.

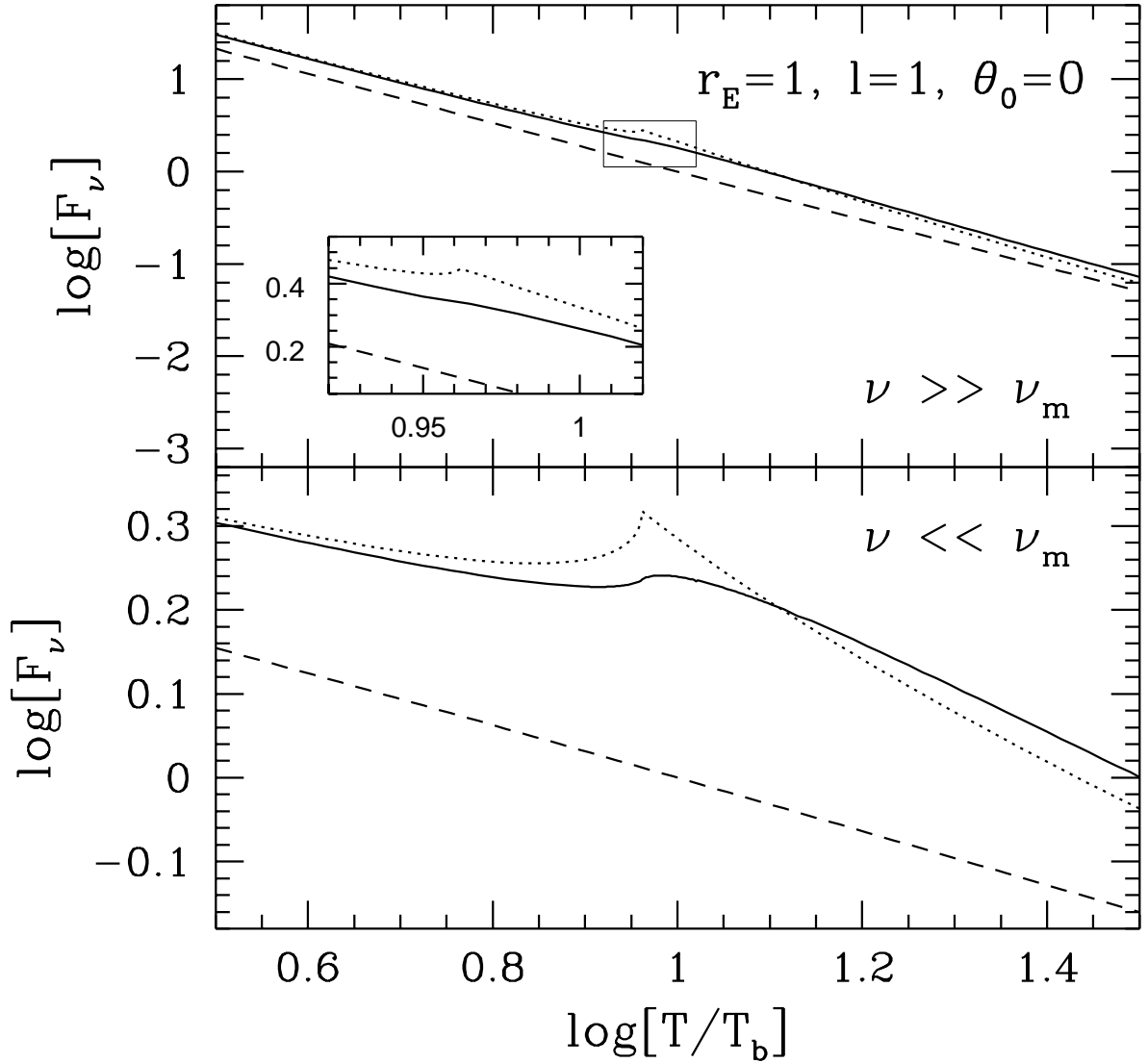


Fig. 3.— The lensed flux of a GRB afterglow, the unlensed flux, and the lensed flux with keeping the initial surface brightness at all the time as a function of the time T are plotted by solid, dashed and dotted lines, respectively. The origin of the vertical axis has no meaning. We set $r_E = 1$, $l = 1$, $\theta_0 = 0$ and $c_s = c/\sqrt{3}$. The upper panel shows the flux at frequencies above the typical synchrotron frequency, and the lower panel is at frequencies below the typical synchrotron frequency. In the upper panel, the boxed region is expanded.

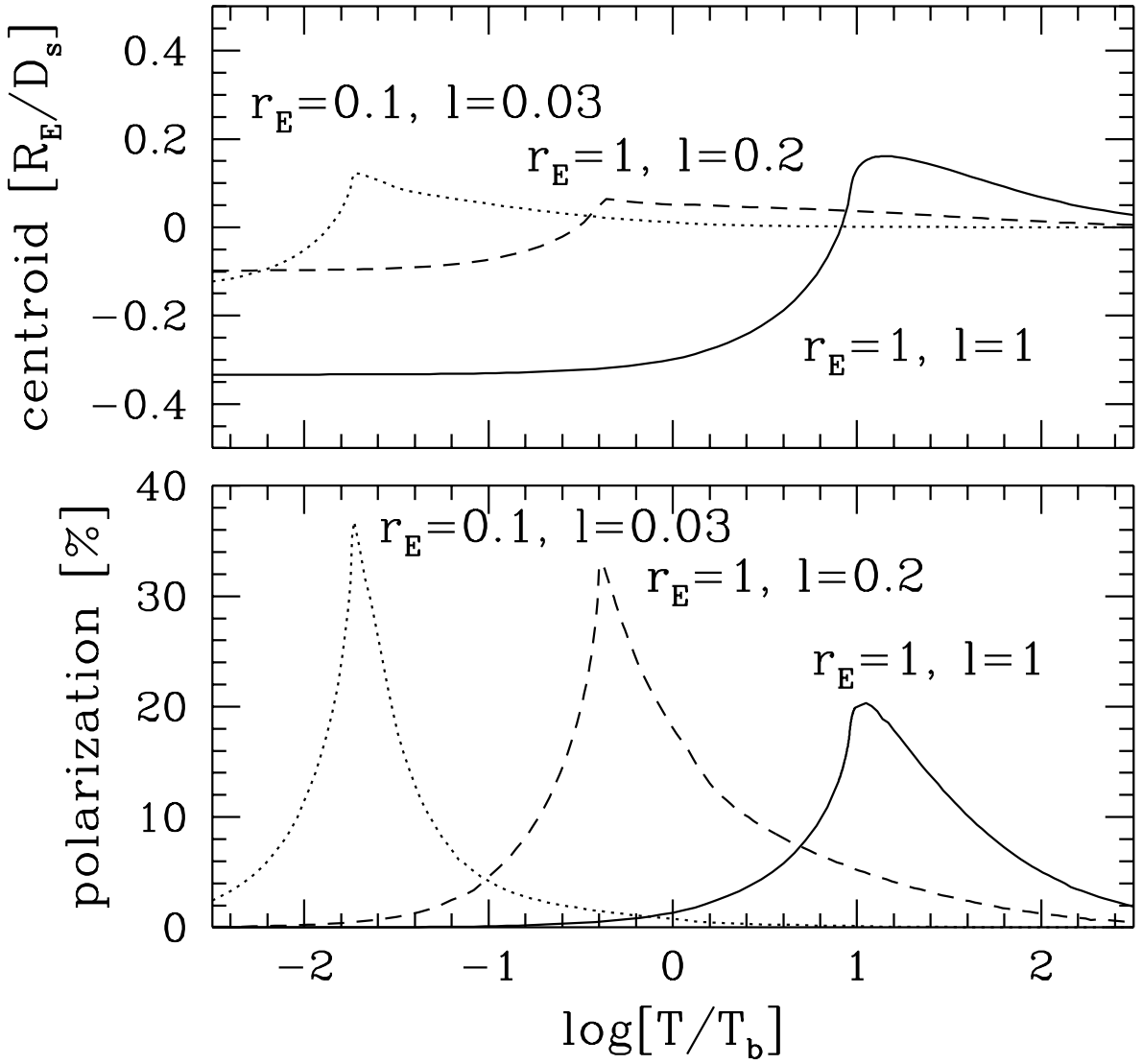


Fig. 4.— In the upper panel, the light centroid position of a GRB afterglow on the sky in units of the ratio of the Einstein radius R_E to the source distance D_s as a function of the time T is shown for three cases $(r_E, l) = (0.1, 0.03), (1, 0.2)$ and $(1, 1)$. The horizontal axis has the same meaning as in the lower panel. In the lower panel, the polarization of a GRB afterglow as a function of the observed time T is shown for $(r_E, l) = (0.1, 0.03), (1, 0.2)$ and $(1, 1)$. The polarization scales linearly with the polarization at each point of the image Π_0 , and we assume here $\Pi_0 = (p + 1)/(p + 7/3) \simeq 72\%$. In both panels, frequencies are above the typical synchrotron frequency.